

Constitutive Manifold Neural Networks

Wouter J. Schuttert , Mohammed Iqbal Abdul Rasheed, Bojana Rosić

Applied Mechanics and Data Analysis, Faculty of Engineering Technology, University of Twente

Abstract

Anisotropic material properties like electrical and thermal conductivities of engineering composites exhibit variability due to inherent material heterogeneity and manufacturing uncertainties. As a tensorial quantity, they are represented as symmetric positive definite tensors, which live on a curved Riemannian manifold, and accurately modelling their stochastic nature requires preserving both their symmetric positive definite properties and spatial symmetries. To achieve this, uncertainties are parametrised into scale (strength) and rotation (orientation) components, modelled as independent random variables on a manifold structure derived from the maximum entropy principle. Further, the propagation of such stochastic tensors through physics-based simulations necessitates computationally efficient surrogate models, like neural networks. However, feedforward neural network architectures are not well-suited for SPD tensors, as directly using the tensor components as inputs fails to preserve their geometric properties, often leading to suboptimal results. To address this, we introduce the Constitutive Manifold Neural Network (CMNN), which is equipped with a preprocessing layer to map the SPD tensor from the curved manifold to the local tangent space, a flat vector space, preserving statistical information in the dataset. A case study on a steady-state heat conduction problem with stochastic anisotropic conductivity demonstrates that geometry-preserving preprocessing, such as logarithmic maps for scale information, significantly improves learning performance over conventional MLPs. These findings underscore the importance of manifold-aware techniques when working with tensor-valued data in engineering applications.

1. Introduction

In advanced materials science, many materials exhibit anisotropic behaviour, where physical properties vary with orientation, such as in composites, biological tissues, or soils [1, 2, 3]. This directional behaviour is inherently captured by mathematical objects called tensors, which describe how key quantities of interest (QoIs) change with spatial direction [4]. Progress in physics-based modelling increasingly relies on methods designed to account for the structure and complexity of anisotropic material tensors, offering potential improvements in predictive efficiency and reducing the risk of costly design or simulation failures [5, 6, 7].

An important class of material tensors is the second-order symmetric and positive definite (SPD) tensor, or SPD matrix, which encodes quantities such as thermal conductivity, electrical conductivity, and magnetic permeability [8]. These properties often vary between specimens due to manufacturing defects or natural phenomena. As a result, accurately predicting material behaviour requires modelling tensor-valued quantities as uncertain [1, 9]. For isotropic second-order properties, this uncertainty can be captured using a scalar-valued random variable. In contrast, for anisotropic materials, the full tensor

must be modelled as a random variable. In this work, we use a parametric stochastic model for second-order SPD tensors recently introduced by Shivanand et al. [10] where the positive definiteness is preserved via the exponential map. The method also separates variation in material properties and orientation through spectral decomposition, allowing for a physics-based interpretation of the tensor-valued random variable.

Introducing uncertain material properties into real-world applications, which may also involve coupled physical processes or multiple spatial scales, often entails a high computational cost. Systems characterised by stochastic material tensors usually contain many degrees of freedom, and integrating over the stochastic space of tensor-valued random variables with classical techniques, such as Monte Carlo, quasi-Monte Carlo or deterministic quadrature, quickly becomes impractical [11, 12, 13].

One way to reduce this burden is to replace the expensive simulator with a surrogate model that approximates the input–output map over the stochastic domain. Surrogate modelling has shown considerable promise for uncertainty propagation [14, 15, 16]. Among the available approaches, neural networks and related deep learning architectures [17] are attractive because they can represent functions in a scalable manner [18]. These networks are usually trained on labelled input–output pairs that cover a prescribed input space. While large data sets enable them to learn complex relationships, data efficiency is critical in physics-based contexts, where numerical simulations are expensive and physical experiments even more so. These constraints motivate the development of more principled, physics-informed network designs that can achieve high accuracy with limited data.

Incorporating physics-based principles into neural networks is not new. Lagrangian neural networks enforce energy conservation through the Euler–Lagrange equations [19, 20], whereas physics-informed neural networks (PINNs) embed partial differential equations in the loss function to avoid explicit solvers [21]. In materials science, where SPD tensors are ubiquitous, constitutive neural networks (CNNs) have been developed to capture stress–strain relations [22, 23, 24]. These models often exploit mechanics-based invariants by tailoring the inputs, outputs or internal architecture. More recently, symmetry-enforcing networks [25] employ eigenvalue activations and rotation-invariant matrices to model symmetric strain behaviour.

Symmetric positive-definite (SPD) tensors form a curved Riemannian manifold because of their symmetry and positive definiteness [26, 27, 28]. Neural networks that recognise this geometry yield more accurate approximations, as seen in SPDNet which maintains the SPD structure by treating weight matrices as manifold points and applying Euclidean activation functions through the logarithmic map [29]. Subsequent work has adapted further Euclidean concepts to the manifold setting: input normalisation via the Fréchet mean [30], residual connections that alleviate vanishing gradients [31], and convolutional operators based on the weighted Fréchet mean [32]. Despite these advances, most methods are developed for large covariance matrices in computer vision and pattern recognition and ignore physical constraints vital to materials science, where for instance eigenvectors encode material orientation [33].

This study investigates surrogate modelling for physics-based simulations that involve uncertain symmetric positive-definite (SPD) material tensors. The focus is on neural network architectures that preserve the geometric structure of SPD data through manifold-aware preprocessing. A case study on a cube-shaped domain with stochastic thermal conductivity and prescribed boundary conditions compares three networks: a conventional multilayer perceptron (MLP), SPDNet, and the newly introduced Constitutive Manifold Neural Network (CMNN). Each model employs a distinct mapping from the SPD manifold to Euclidean space. By evaluating their performance under different forms of uncertainty, we show that geometry-aware networks improve approximation accuracy and training stability.

The paper is structured as follows. The necessary physics and the modelling of stochastic parametric tensors are introduced in Section 2. Section 3 presents the preprocessing methods developed for neural

networks to handle SPD tensorial data effectively. In Section 4, a case study with three different types of uncertainty are modelled namely, scaling, orientation, and a combination of both. Subsequently, the neural networks introduced in Section 3 are evaluated for their approximation performance. Section 5 draws conclusions from the results, discusses limitations, and proposes directions for future research.

2. Stochastic heat transfer

Assume a physical system undergoing heat conduction described by the following elliptic partial differential equations (PDE):

$$-\nabla \cdot (\mathbf{C} \nabla T(\mathbf{x})) = Q(\mathbf{x}) \quad \text{a.e. in } \mathcal{G}, \quad (2.1)$$

with boundary conditions

$$T(\mathbf{x}) = T_D(\mathbf{x}) \quad \text{on } \Gamma_D \subseteq \partial \mathcal{G}, \quad (2.2)$$

$$-\mathbf{C} \nabla T(\mathbf{x}) \cdot \vec{n} = Q_N(\mathbf{x}) \quad \text{on } \Gamma_N \subseteq \partial \mathcal{G}, \quad (2.3)$$

in which the bounded domain $\mathcal{G} \subset \mathbb{R}^d$ resides in d -dimensional Euclidean space, with $d = 2$ or $d = 3$. Within this domain, the temperature at each point $\mathbf{x} \in \mathcal{G}$ is represented by $T(\mathbf{x})$, while the source term $Q(\mathbf{x})$ accounts for thermal sources or sinks. On the Dirichlet boundary Γ_D , the temperature is prescribed by $T_D(\mathbf{x})$, while on the Neumann boundary Γ_N , the heat flux through the surface is specified as $Q_N(\mathbf{x})$. The physical system is parametrised by a thermal conductivity tensor belonging to a space of symmetric and positive-definite (SPD) matrices, i.e.

$$\mathbf{C} \in \text{Sym}^+(d) := \left\{ \mathbf{C} \in (\mathbb{R}^d \otimes \mathbb{R}^d) \mid \mathbf{C} = \mathbf{C}^T, \mathbf{z}^T \mathbf{C} \mathbf{z} > 0, \forall \mathbf{z} \in \mathbb{R}^d \setminus \{\mathbf{0}\} \right\}, \quad (2.4)$$

here assumed to be spatially homogeneous and anisotropic. Positive definiteness ensures that energy conservation principles are maintained, while symmetry captures the balanced interactions within a material governed by Onsager's reciprocal relations [34]. Due to these properties, the conductivity tensor does not belong to a Euclidean space but an open convex cone within the space of symmetric matrices $\text{Sym}(d)$. This open convex cone forms a Riemannian manifold, a curved space that locally resembles Euclidean space \mathbb{R}^d in its tangent space. The local resemblance is formalised through continuous (homeomorphic) and differentiable (diffeomorphic) mappings between the manifold and its tangent space, enabling the use of calculus on the manifold [35].

In real applications, \mathbf{C} is unknown and thus has to be estimated given experimental observations of the temperature field. In practice, without measurements, \mathbf{C} must be prescribed a priori based on previous expert knowledge, by modelling \mathbf{C} as a symmetric and positive-definite tensor-valued random variable that represents epistemic uncertainty in the conductivity tensor. Let $(\Omega, \mathcal{F}, \mathbb{P})$ be the probability space in which Ω is the set of all elementary events ω , \mathcal{F} is the sigma algebra, and \mathbb{P} is the probability measure. Then $\mathbf{C}(\omega)$ can be modelled as a finite variance SPD-valued random variable in $L_2((\Omega, \mathcal{F}, \mathbb{P}), \text{Sym}^+(d))$. As a consequence, the deterministic PDE in Eq.(2.1) becomes stochastic,

$$-\nabla \cdot (\mathbf{C}(\omega) \nabla T(\mathbf{x}, \omega)) = Q(\mathbf{x}) \quad \text{a.e. in } \mathcal{G}, \text{ and a.s. } \omega \in \Omega, \quad (2.5)$$

with boundary conditions

$$T(\mathbf{x}, \omega) = T_D(\mathbf{x}) \quad \text{on } \Gamma_D \subseteq \partial \mathcal{G}, \forall \omega \in \Omega, \quad (2.6)$$

$$-\mathbf{C}(\omega) \nabla T(\mathbf{x}, \omega) \cdot \vec{n} = Q_N(\mathbf{x}) \quad \text{on } \Gamma_N \subseteq \partial \mathcal{G}, \forall \omega \in \Omega. \quad (2.7)$$

As a result, the temperature field $T(\mathbf{x}, \omega)$ is a finite variance random field in $L_2((\Omega, \mathcal{F}, \mathbb{P}), H^1(\mathcal{G}))$, where H^1 is the first-order Sobolev space.

The main goal of this study is to quantify the uncertainty in $T(\mathbf{x}, \omega)$ given a known description of $\mathbf{C}(\omega)$. As a probabilistic description of $\mathbf{C}(\omega)$ is not straightforward due to the non-Euclidean structure, we first present a model for the parameter space, and then outline the procedure required for quantifying the uncertainty in of the temperature field $T(\mathbf{x}, \omega)$.

2.1. Stochastic anisotropic thermal conductivity tensor

As outlined in [10], a stochastic SPD tensor $\mathbf{C}(\omega)$ must satisfy three key properties. First, it must be SPD for all $\omega \in \Omega$. Second, it must exhibit invariance under a subgroup $G \subset O(\mathbb{R}^d)$ of orthogonal transformations, satisfying $\mathbf{R}^T \mathbf{C}(\omega) \mathbf{R} = \mathbf{C}(\omega)$ for all $\mathbf{R} \in G$ and $\omega \in \Omega$. Lastly, the mean tensor $\overline{\mathbf{C}} := \mathbb{E}_\vartheta(\mathbf{C}(\cdot))$ must remain invariant under a broader group $G_m \subseteq O(\mathbb{R}^d)$, including transformations such as inversion, scaling, and frame changes.

To facilitate the modelling of the stochastic material tensor under these requirements, we adopt an eigenvalue decomposition approach [10]. A conductivity tensor \mathbf{C} can be decomposed into its eigenvalues and eigenvectors:

$$\mathbf{C} = \mathbf{Q} \mathbf{\Lambda} \mathbf{Q}^T, \quad (2.8)$$

where $\mathbf{Q} \in \text{SO}(d)$ represents the eigenvectors in the special orthogonal group, and $\mathbf{\Lambda} \in \text{Diag}^+(d)$ represents the eigenvalues in the space of positive-definite diagonal matrices, which is a Lie group under matrix multiplication. The eigenvectors \mathbf{Q} represent the principal directions of material symmetry, while the eigenvalues $\mathbf{\Lambda}$ reflect the material properties, such as conductivity along these principal directions.

To incorporate stochastic variations in the material tensor, we account for uncertainty in both $\mathbf{\Lambda}(\omega)$ and $\mathbf{Q}(\omega)$. However, since these quantities reside on manifolds, linear algebra cannot be applied directly [36]. Instead, we express $\mathbf{\Lambda}(\omega)$ and $\mathbf{Q}(\omega)$ in their respective Lie algebras (\mathbf{Y}, \mathbf{W}) , in which $\mathbf{Y} \in \mathfrak{diag}(d)$ is the space of diagonal matrices, and $\mathbf{W} \in \mathfrak{so}(d)$ is the space of skew-symmetric matrices. To map the Lie algebras, we then have

$$(\mathbf{Y}, \mathbf{W}) \mapsto (\mathbf{\Lambda}, \mathbf{Q}) = (\exp \mathbf{Y}, \exp \mathbf{W}) \mapsto \mathbf{C} = \mathbf{Q} \mathbf{\Lambda} \mathbf{Q}^T, \quad (2.9)$$

i.e.

$$\mathfrak{diag}(d) \times \mathfrak{so}(d) \xrightarrow{\exp \times \exp} \text{Diag}^+(d) \times \text{SO}(d) \longrightarrow \text{Sym}^+(d). \quad (2.10)$$

In this manner, we satisfy the first and second requirements. To satisfy the third requirement, we adopt the scaling-rotation metric for the Fréchet mean, the generalised definition of the mean commonly used on the SPD manifold. For further details, the reader is referred to [37, 10].

With all three requirements satisfied, the symmetric positive-definite tensor-valued random variable is described as

$$\mathbf{C}(\omega) = \exp(\mathbf{W}(\omega)) \overline{\mathbf{Q}} \exp(\mathbf{Y}(\omega)) \overline{\mathbf{Q}}^T \exp(\mathbf{W}(\omega)^T), \quad \forall \omega \in \Omega, \quad (2.11)$$

where $\exp(\mathbf{W}(\omega))$ around the reference eigenvector $\overline{\mathbf{Q}}$ models the random eigenvector matrix $\mathbf{Q}(\omega)$. The random rotation matrix is modelled as

$$\mathbf{W} = \text{skw}(\mathbf{w}) = \begin{bmatrix} 0 & -w_3 & w_2 \\ w_3 & 0 & -w_1 \\ -w_2 & w_1 & 0 \end{bmatrix}, \quad \mathbf{W} = -\mathbf{W}^T. \quad (2.12)$$

This can be further written as:

$$\mathbf{w} = \phi \mathbf{r}, \quad \mathbf{r} \cdot \mathbf{r} = 1 \quad (2.13)$$

such that

$$\mathbf{W} = \phi \mathbf{R}, \quad \mathbf{R} := \text{skw}(\mathbf{r}) \quad (2.14)$$

where ϕ is the rotation angle. The randomness is then modelled by taking this angle to be drawn from a von Mises–Fisher distribution (vMF) [38].

$$f(\phi; \boldsymbol{\mu}, \eta) = C_p(\eta) \exp(\eta \boldsymbol{\mu}^T \phi) \quad (2.15)$$

where $\boldsymbol{\mu}$ is the mean vector, η the concentration parameter (akin to the standard deviation of a normal distribution), and C_p is a normalization constant which ensures the distribution lies on the unit sphere. The vMF is a generalization of a Gaussian distribution to the unit sphere and adheres to the principle of maximum entropy [39, 40]. The stochastic eigenvalue matrix $\mathbf{Y}(\omega)$, also chosen according to the principle of maximum entropy, is modelled as a tensor-valued random variable.

$$\mathbf{Y}(\omega) = \text{diag}(y_i(\omega)) \quad \text{with} \quad y_i(\omega) \sim \mathcal{N}(\mu_i, \sigma_i^2), \quad i = 1, \dots, d, \quad (2.16)$$

where the subscript i refers to the i^{th} diagonal term of the eigenvalue matrix. Note that the exponential map of a Gaussian random variable corresponds to directly modelling a log-normal random variable at every diagonal element in the matrix $\mathbf{\Lambda}(\omega)$.

Together, the probabilistic models for scaling and orientation allow for the necessary choice in symmetry classes by choosing the number of independent eigenvalues, i.e., isotropy with a single independent eigenvalue, or orthotropy with three in \mathbb{R}^3 . Meanwhile, depending on the number of varying symmetry planes through the random rotation matrix different types of symmetry can be set.

2.2. Discretization and Approximation of the Temperature Field

The problem described in Eq.(2.5) is continuous and must be further discretised. For the spatial discretisation, we use the Finite Element Method by choosing $\mathcal{G} = \bigcup_e T_e$, in which T_e denotes the corresponding elements. Within each element, the solution is approximated using a finite set of basis functions:

$$\mathbf{T}(\mathbf{x}, \omega) = \sum_{i=1}^M T_i(\omega) N_i(\mathbf{x}), \quad (2.17)$$

here, the function $\mathbf{T}(\mathbf{x}, \omega)$ is expressed as a linear combination of basis functions $N_i(\mathbf{x})$, weighted by the stochastic coefficients $T_i(\omega)$. Since this formulation only discretises the spatial domain, the resulting system remains continuous in the probabilistic space and requires further stochastic discretisation. For this purpose, we employ the Monte Carlo (MC) sampling technique:

$$\mathbf{T}(\mathbf{x}, \omega_j) = \sum_{i=1}^M T_i(\omega_j) N_i(\mathbf{x}), \quad j = 1 \dots N, \quad (2.18)$$

where, at each nodal point, we collect values of the temperature through N samples of the probability space, indicated by ω_j .

MC estimation is a computationally costly technique when combined with the Finite Element Method. Instead, we aim to utilise only part of the generated data to formulate a surrogate model. The goal is to compute the quantity of interest (temperature field), i.e. the mapping:

$$F : L_2((\Omega, \mathcal{F}, \mathbb{P}), \text{Sym}^+) \rightarrow L_2((\Omega, \mathcal{F}, \mathbb{P}), H^1(\mathcal{G})) \quad (2.19)$$

such that

$$y(\mathbf{C}(\omega)) = F(\mathbf{C}(\omega); \theta), \quad (2.20)$$

holds. The goal is to learn parameters θ given the collected MC data.

3. Constitutive Manifold Neural Networks

In the previous equation, F is assumed to be an abstract continuous and measurable mapping. For computational purposes, we choose a family of neural networks as the approximating functions, specifically a feedforward neural network architecture suited to the problem. Let \mathbf{q} be a vectorised version of the tensor \mathbf{C} . Then, the QoI in Eq.(2.20) is approximated by

$$\hat{y}(\mathbf{q}) \approx H_\theta(\mathbf{q}) = (A^L \circ f_a^L \dots \circ f_a^{l_2} \circ A^{l_2} \circ f_a^{l_1} \circ A^{l_1})(\mathbf{q}), \quad (3.1)$$

where a conventional affine map is given by

$$A^{l_k}(\mathbf{q}^{l_k}) = \mathbf{W}^{l_k} \mathbf{q}^{l_k} + \mathbf{b}^{l_k}. \quad (3.2)$$

Here, $A^{l_k} : \mathbb{R}^{n^{l_{k-1}}} \rightarrow \mathbb{R}^{n^{l_k}}$ represents the affine operation at depth k , with $k = l_1, l_2, \dots, L$ being the layers, while $\mathbf{q}^{l_k} \in \mathbb{R}^{n^{l_k}}$ is the input vector coming from layer l_{k-1} , n^{l_k} is the size of layer k and $f_a^{l_k}$ is the activation function. Together, the weights $\mathbf{W}^l \in \mathbb{R}^{n^{l_k} \times n^{l_{k-1}}}$ and biases $\mathbf{b}^{l_k} \in \mathbb{R}^{n^{l_k}}$ parameterise the linear operations in each layer, and together with activation functions enable the network to approximate the target function.

While the previous approximation is commonly used in engineering practice, it is unfortunately inadequate in the context of stochastic symmetric positive-definite tensors. Specifically, it relies on mapping parameters that reside on a nonlinear manifold to the quantity of interest (QoI) using classical algebraic operations called vectorisation or flattening, an approach that fails to capture the underlying geometric structure of the parameter space. While this embedding enables the use of standard neural network architectures, it imposes a Euclidean geometry on inherently non-Euclidean data [41]. Specifically, vectorisation induces the flat norm,

$$d_{\text{vec}}(\mathbf{C}_1, \mathbf{C}_2) = \|\mathbf{C}_1 - \mathbf{C}_2\|_F. \quad (3.3)$$

which treats SPD tensors as elements of a flat Euclidean space, ignoring the geometry of the manifold. This distortion introduces additional nonlinearity into the data representation and undermines standard computations, such as those for the mean or variance, which are no longer meaningful under this metric [27]. A neural network is trained to operate under the assumption that such distances between samples are meaningful in the Euclidean sense. Consequently, the distortions imposed by the flat metric in Eq.(3.3) can severely limit the network's ability to learn the desired functional relationships [42, 43, 29].

To accommodate working with an SPD tensor from $\mathbf{C}(\omega) \in L_2((\Omega, \mathcal{F}, \mathbb{P}), \text{Sym}^+)$, rather than vectors \mathbf{q} , we introduce a preprocessing layer $B : \text{Sym}^+(d) \rightarrow \mathbb{R}^{n^{l_0}}$. This layer maps from the manifold of SPD tensors to a Euclidean space which serves as input to the hidden layers of the neural network, leading to the formulation of a Constitutive Manifold Neural Network (CMNN):

$$\hat{y}(\mathbf{C}) = F_\theta(\mathbf{C}) = (A^L \circ f_a^L \dots \circ f_a^{l_2} \circ A^{l_2} \circ f_a^{l_1} \circ A^{l_1} \circ B)(\mathbf{C}). \quad (3.4)$$

The network F_θ provides a parametric approximation of the target mapping defined in Eq.(2.19). In this work, we focus on introducing two alternative versions for B instead of vectorization that respect the manifold structure, thereby potentially capturing the relationship between the stochastic material tensor and the random temperature field more effectively.

The first alternative is inspired by a widely used Riemannian metric for SPD tensors, the Log-Euclidean metric [41], defined as

$$d_{LE}(\mathbf{C}_1, \mathbf{C}_2) = \|\log(\mathbf{C}_1) - \log(\mathbf{C}_2)\|_F, \quad (3.5)$$

where the matrix logarithm $\log(\mathbf{C}) = \mathbf{Q} \log(\mathbf{\Lambda}) \mathbf{Q}^\top$ maps tensors to the tangent space of symmetric matrices. This metric respects the manifold geometry, contrasting with the flat Euclidean metric induced by vectorization. To integrate the metric into a neural network, we utilise the log-eigenvalue operation (LogEig) as a geometry-aware preprocessing layer, first introduced in SPDNet [29]. The LogEig operation, i.e. the mapping

$$E : \text{Sym}^+(d) \xrightarrow{\log} \text{Sym}(d) \xrightarrow{\text{flat}} \mathbb{R}^{d(d+1)/2}. \quad (3.6)$$

maps the eigenvalues into the Lie algebra \mathfrak{diag} via a logarithmic map and reconstructs it in the linear space $\text{Sym}(d)$. While computationally effective, this approach is known to introduce swelling, fattening, and shrinking effects when applied to SPD tensors [44, 45].

The second approach, inspired by the scaling-rotation metric, mitigates geometric distortions while remaining computationally efficient [37, 10]. The scaling-rotation metric is defined as

$$d_{sr}(\mathbf{C}_1, \mathbf{C}_2) = \sqrt{d_L(\mathbf{\Lambda}_1, \mathbf{\Lambda}_2)^2 + c d_R(\mathbf{Q}_1, \mathbf{Q}_2)^2} \quad (3.7)$$

where

$$d_L(\mathbf{\Lambda}_1, \mathbf{\Lambda}_2) = \|\log(\mathbf{\Lambda}_1) - \log(\mathbf{\Lambda}_2)\|_F, \quad d_R(\mathbf{Q}_1, \mathbf{Q}_2) = \|\log(\mathbf{Q}_1^\top \mathbf{Q}_2)\|_F. \quad (3.8)$$

This metric decomposes the distance into a scaling part, d_L , represented by the eigenvalues $\mathbf{\Lambda}_i$, and a rotation part, d_R , captured through the eigenvectors \mathbf{Q}_i of the SPD tensors. The parameter $c > 0$ balances these components by controlling the trade-off between scale and orientation alignment.

To leverage this metric in neural networks, we propose feeding the network separate strength and orientation information, referred to as the strength-angular (StrAng) layer. The StrAng layer decomposes the tensor into eigenvalues and eigenvectors, applies logarithmic scaling to the eigenvalues and eigenvectors, and flattens both components into a Euclidean vector through the following map S ,

$$S := (\varrho^{\text{eig}} \circ \varrho^{\log} \circ \varrho^{\text{flat}}) \quad (3.9)$$

where

$$\varrho^{\text{eig}} := \text{Sym}^+(d) \xrightarrow{\text{eig}} \text{Diag}+(d) \times \text{SO}(d) \quad (3.10)$$

$$\varrho^{\log} := \text{Diag}+(d) \times \text{SO}(d) \xrightarrow{(\log, \log)} \mathfrak{diag}(d_1) \times \mathfrak{so}(d_2) \quad (3.11)$$

$$\varrho^{\text{flat}} := \mathfrak{diag}(d_1) \times \mathfrak{so}(d_2) \xrightarrow{\text{flat}} \mathbb{R}^{(d_1+d_2)} \quad (3.12)$$

Here, d_1 denotes the number of independent eigenvalues, which are flattened into d_1 entries, while d_2 is the number of random angles flattened into d_2 entries, both are dependent on the type of symmetry and anisotropy class, i.e. $(d_1, d_2) = (3, 3)$ for fully anisotropic materials or $(d_1, d_2) = (1, 0)$ for isotropic materials. The map ϱ^{eig} computes the eigen-decomposition and, as in the scaling-rotation metric, keeps the eigenvalues and eigenvectors separate. Using ϱ^{\log} , we apply the matrix logarithm to map the eigenvalues from the open convex cone of positive-definite matrices to the flat tangent space. Similarly, the eigenvectors are mapped to their tangent space \mathfrak{so} as angles. Finally, ϱ^{flat} creates a representation in \mathbb{R} from the eigenvalues and eigenvectors. Regardless of choice for B , the weights and biases of the CMNN are trained by minimising the discrepancy between the true operator F and F_θ . Since both are

defined over a probability space $(\Omega, \mathcal{F}, \mathbb{P})$, the training objective takes the form of an expected error in the Bochner space $L^2((\Omega, \mathcal{F}, \mathbb{P}), H^1(\mathcal{G}))$:

$$\mathcal{L}(\theta) = \mathbb{E}_{\omega \sim \mathbb{P}} \left[|F_\theta(\mathbf{C}(\omega)) - F(\mathbf{C}(\omega))|_{H^1(\mathcal{G})}^2 \right]. \quad (3.13)$$

While the theoretical objective is formulated in $L^2((\Omega, \mathcal{F}, \mathbb{P}), H^1(\mathcal{G}))$ to capture both functional and gradient-level discrepancies, in practice we train the network using a standard mean squared error (MSE) loss over discretised output representations defined as,

$$\hat{\mathcal{L}}(\theta) = \frac{1}{N} \sum_{i=1}^N |\hat{y}(\mathbf{C}_i; \theta) - T_i|^2, \quad (3.14)$$

where $\{(\mathbf{C}_i, T_i)\}_{i=1}^N$ are sampled input-output pairs from the data distribution. The MSE loss avoids the need to compute spatial derivatives of the network output, which is challenging in the implicit representation obtained by neural networks. For updating the weights and biases the backpropagation algorithm remains unchanged since the input transformations do not interfere with the internal architecture of the feedforward neural network.

Lastly, we require a unique spectral decomposition for the StrAng and LogEig layers, as the decomposition is inherently non-unique. Eigenvectors can change sign arbitrarily, and the ordering of the eigenvalues can vary, yet the decomposition remains valid. Despite this mathematical flexibility, such ambiguities can lead to inconsistencies when considering the physical interpretation of the material. To address this issue, we adopt a sorting algorithm that resolves both the sign and permutation ambiguities of eigenvectors and eigenvalues by aligning them with the reference tensor $\overline{\mathbf{C}} = \overline{\mathbf{Q}} \overline{\mathbf{\Lambda}} \overline{\mathbf{Q}}^T$. This alignment is achieved by solving the following minimisation problem,

$$(P^*, S^*) = \underset{P \in \mathcal{P}, S \in \mathcal{S}}{\operatorname{argmin}} d(P, S) \quad \text{where} \quad d = d_R(\mathbf{Q}, \overline{\mathbf{Q}}), \quad (3.15)$$

where $P \in \mathcal{P}$ represents one of the six possible permutations of the eigenvalue indices, $S \in \mathcal{S}$ represents one of the eight possible sign configurations for the eigenvector columns, and $d_R(P, S)$ is a cumulative distance measure between eigenvectors after applying the respective permutations and sign changes. The objective is to find the configuration (P^*, S^*) that minimises $d(P, S)$ while ensuring eigenvectors align with $\overline{\mathbf{C}}$. This alignment is robust for rotations up to a 45° deviations from the initial eigenvectors, well beyond the typical variations observed in advanced materials.

4. Case Study

To investigate the performance of the proposed neural networks in handling anisotropic SPD material data, we analyse steady-state heat conduction in a patched cube with anisotropic and uncertain thermal conductivity, governed by Eq.(2.5). The patched cube is chosen for its direction-dependent geometry, consisting of six patches, each oriented along one of the Cartesian axes with normals aligned to the cube's faces. The cube has a side length of 0.05 m, with each patch measuring 0.005 m. The geometry is shown in Fig.(1a), where a red patch on one YZ face indicates a Neumann boundary condition, $Q_N = 50 \text{ kW/m}^2$, while the other five patches (blue) are subject to a Dirichlet boundary condition, $T_D = 273.15 \text{ K}$. The remaining boundary is insulated. The figure also features a cutout that shows the direction of the fibres within the cube. To parameterise the anisotropic thermal properties, we consider a deterministic thermal conductivity tensor representative of unidirectional stacked composites [46]. These composites are used in lightweight, load-bearing structures and exhibit distinct thermal properties in three principal directions:

fibre, stacking, and transverse. The thermal conductivity tensor, its eigenvalues, and eigenvectors are given by:

$$\mathbf{C} = \begin{bmatrix} 11.24 & 5.18 & 1.73 \\ 5.18 & 3.49 & -0.356 \\ 1.73 & -0.356 & 1.78 \end{bmatrix} \text{ where } \mathbf{\Lambda}_\kappa = \begin{bmatrix} 14 \\ 0.11 \\ 2.4 \end{bmatrix} \text{ and } \mathbf{Q}_\kappa = \begin{bmatrix} 0.892 & -0.416 & 0.174 \\ 0.436 & 0.700 & 0.565 \\ 0.113 & 0.580 & 0.807 \end{bmatrix}. \quad (4.1)$$

The first eigenvalue captures the high conductivity along the fibre direction, due to the fibre-dominant thermal properties of the material. The second eigenvalue reflects the lower conductivity in the out-of-plane stacking direction, influenced by thicker plastic composite layers between tapes. The third eigenvalue represents the in-plane transverse conductivity, which is higher than in the stacking direction due to a more uniform fibre and polymer distribution. A dense rotation matrix, defined by Euler angles of 35° , 10° , and 25° , introduces pronounced interactions between material orientation and cube geometry, capturing complex anisotropic behaviour of the material.

To solve the deterministic case for $T(\mathbf{x})$, as described in Eq.(2.1), spatial discretisation is carried out using the approach outlined in Eq.(2.17). The simulation is performed in the commercial software COMSOL Multiphysics® [47], where the geometry is discretised into approximately 16,000 quadratic Lagrangian tetrahedral elements e , sharing about 3,000 nodal points, as shown in Fig.(1b). The Generalized Minimum Residual (GMRES) method is employed to solve the resulting system of equations.

The deterministic solution, obtained using Eq.(4.1), is shown in Fig.(1c). The results clearly demonstrate that the fibre direction significantly influences heat transport, directing it along principal paths. Fig.(2) depicts the XY, XZ, and YZ planes, where boundary conditions create temperature gradients, with a noticeable drop near the patches where $T = T_b$. The highest temperature occurs at the heat source boundary, as expected. The projections of the 3D vectors onto the 2D planes visualise the principal directions of thermal conductivity, further revealing the fibre direction within the planes. Short vectors indicate directions with minimal in-plane projection, typically associated with lower effective conductivity in that plane. This deterministic reference sets the stage for evaluating the effect of uncertainty in the conductivity tensor on the temperature field.

To evaluate the variability in the temperature field, we use $N = 500,000$ samples and compute the

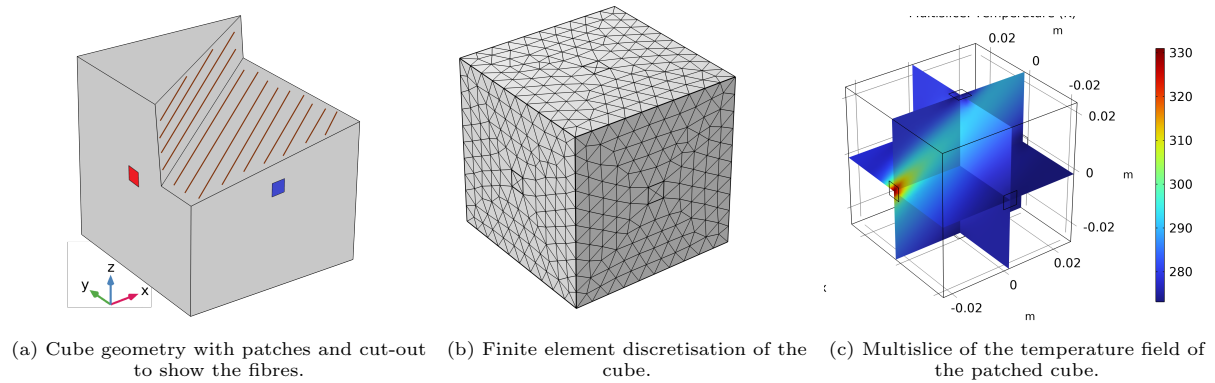


Figure 1: Simulation domain and deterministic result.

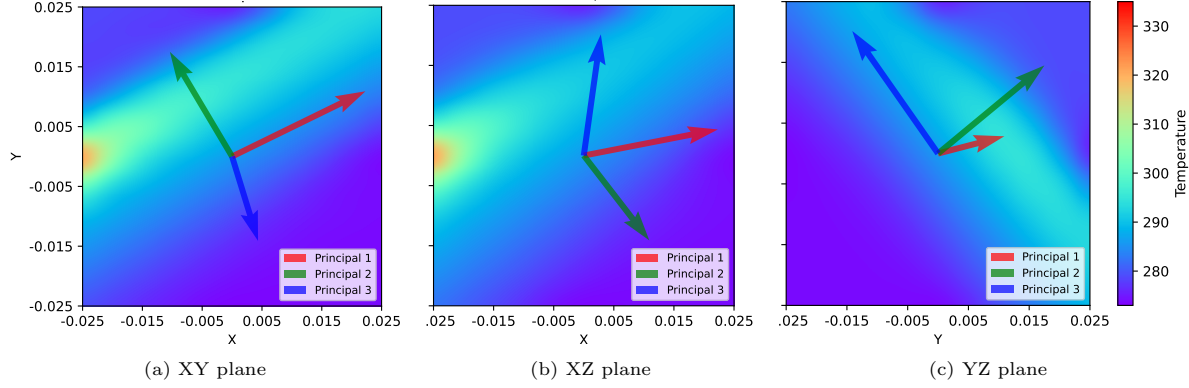


Figure 2: Deterministic temperature field for the multi-slice planes with projection of principal directions.

mean μ_T and standard deviation σ_T using the Monte Carlo formulation in Eq.(2.18), as follows:

$$\mu_T \approx \frac{1}{N} \sum_{j=1}^N T_i(\omega_j), \quad \sigma_T \approx \sqrt{\frac{1}{N-1} \sum_{j=1}^N (T_i(\omega_j) - \mu_T)^2}, \quad (4.2)$$

for a single solution point i . To estimate the probability distribution function, Kernel density estimation (KDE) is employed as a non-parametric method to approximate the probability density function $f(T_i)$ from data samples $T_i(\omega_1), T_i(\omega_2), \dots, T_i(\omega_N)$, defined as

$$\hat{f}(T_i) = \frac{1}{Nh} \sum_{j=1}^N K\left(\frac{T_i - T_i(\omega_j)}{h}\right). \quad (4.3)$$

Here, $K(u)$ is the kernel function, chosen as a Gaussian kernel $K(u) = \frac{1}{\sqrt{2\pi}} e^{-u^2/2}$. The bandwidth h is computed using Scott's rule: $h = \sigma \cdot N^{-1/5}$.

4.1. Surrogate modelling of a patched cube with stochastic thermal conductivity

In the following, we compare the generalisation performance of the proposed MLP, SPDNet, and CMNN architectures using standard vectorization, Eq.(3.6), and Eq.(3.9) as preprocessing steps for B in Eq.(3.4), respectively, when handling uncertain anisotropic material tensors. To facilitate the machine learning analysis, the temperature field is reduced to a coarser, equally-spaced grid of $11 \times 11 \times 11$ points over the cube, chosen to balance computational cost and data fidelity. For visualisation and further data processing, the temperature values at these grid points are interpolated to enhance the smoothness and readability of the visualised temperature distribution.

Each network is trained with 16,000 samples, validated with 4,000 samples, and tested on 30,000 samples, which represent only a tenth of the reference Monte Carlo (MC) set. The hidden layers, layer sizes, activation functions, number of epochs, batch size, and learning rate are determined through Bayesian hyperparameter optimization using a tree-structured Parzen estimator [48]. For each network, training is repeated across 10 experiments with different initial sample configurations and network initializations.

To analyse the expected error at a grid point, we examine the sample-average normalised norms:

$$\ell_p = \mathbb{E} \left[\frac{\|T(x, \omega_i) - \hat{T}(x, \omega_i)\|_p}{\|T(x, \omega_i)\|_p} \right] \quad (4.4)$$

which provide insight into the expected error at a single grid point in the solution field. Specifically, for $p = 1$, this metric computes the expected relative difference between the predicted and finite element temperature fields, offering a measure of the average deviation. When $p = 2$, larger errors are emphasised, while for $p = \infty$, the worst-case scenario is produced. Norms are computed on a random temperature field, the mean temperature field and the standard deviation field.

Furthermore, to assess local errors across the entire temperature field, the absolute δT_a and relative T_r errors at each point are computed as:

$$\delta T_a = |\hat{T}_i - T_i|, \quad \delta T_r = \frac{|\hat{T}_i - T_i|}{|T_i|}, \quad (4.5)$$

allowing for the visualisation of error distributions across an entire data slice using colour maps. Here, we restrict our analysis to the XY perspective, as Fig.(2a) provides insight into the boundary conditions and the first principal direction.

Lastly, the Kullback–Leibler (KL) divergence quantifies the difference between the predicted and reference probability density functions. This metric evaluates how closely the predicted distributions align with the reference data:

$$D_{\text{KL}} = \sum_{j=1}^k P_j \log \left(\frac{P_j}{Q_j} \right), \quad (4.6)$$

where P_j and Q_j represent the probabilities from the reference and predicted histograms, respectively.

4.1.1. Surrogate model for scaling uncertainty

To evaluate networks' performance under scaling uncertainty, we define a tensor-valued random variable using Eq.(2.11), with three independent log-normal random variables. The mean values, μ_i , are derived from Eq.(4.1), while the standard deviations are chosen to reflect uncertainties observed in composites [49, 50]. Table 1 lists the mean and standard deviation for the log-normal variables.

The statistical characteristics of the temperature field under scaling uncertainty are depicted in Fig.(3). The mean temperature field, shown in Fig.(3a), is similar to that of the deterministic solution, as expected. The standard deviation of the temperature field, presented in Fig.(3b), mirrors regions of high mean temperature, indicating that hotter regions exhibit greater variability. Fig.(3c) shows the probability-density functions (PDFs) of the temperature at two selected points, marked in Fig.(3a). The PDF in the high-temperature region (red) exhibits a shifted mean compared to the cooler region (blue), consistent with heat conduction. Furthermore, both points display non-normal distributions seen in the shape of top of the curve, although their spreads and peak sharpness differ slightly.

Table 1: Parameters of the log-normal random variables.

Variable	Mean (μ)	Standard Deviation (σ)
c_1	14.0	0.8
c_2	0.11	0.02
c_3	2.4	0.27

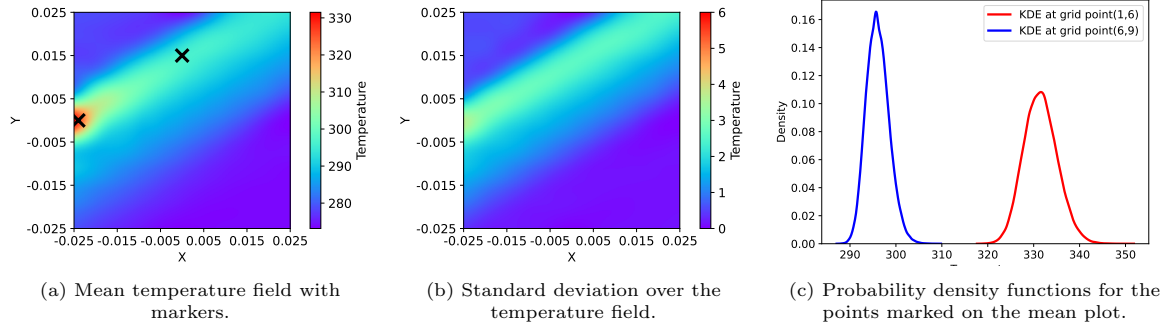


Figure 3: Temperature field statistics in the XY plane with the scaling uncertainty dataset.

To train the MLP, SPDNet, and CMNN, the optimised hyperparameters are 300 epochs, a batch size of 8, two hidden layers with 16 and 8 neurons, a Tanh activation function, the Adam optimizer, and a learning rate of 3×10^{-3} . Table 2 compares the performance of the MLP, SPDNet, and CMNN architectures on the scaling dataset. The MLP architecture struggles to generalize, exhibiting a high validation loss (2.16×10^4). In contrast, the SPDNet and CMNN architectures demonstrate much lower validation losses (0.20×10^4 and 0.30×10^4 , respectively). SPDNet achieves the most consistent performance, with the smallest mean and standard deviation across repeated experiments, while CMNN delivers competitive results but with slightly higher variability. A similar trend is visible in Table 3; notably, SPDNet outperforms the CMNN in estimating the standard deviation. Instabilities are further evident in the training histories depicted in Fig.(4), where validation losses for the MLP (Fig.(4a)) and,

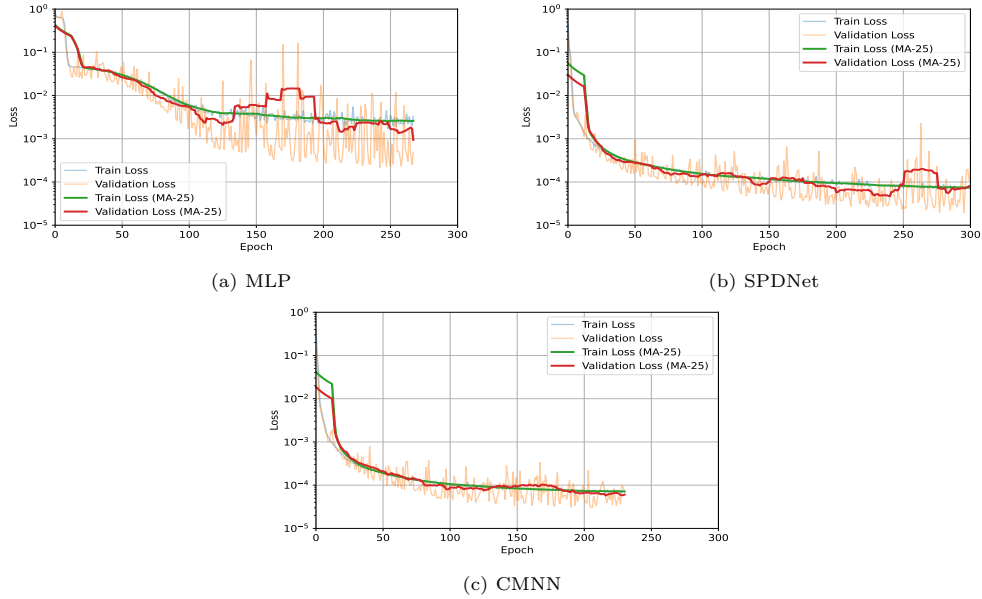


Figure 4: Training history of the neural networks with the scaling uncertainty dataset.

Table 2: Training metrics of the neural networks with the scaling uncertainty dataset. Data in magnitude order of e^{-4} .

Layer	Best Loss	Val. Test Loss	Train Loss	Mean Val. Loss (Std.)	Mean Test Loss (Std.)	Mean Train Loss (Std.)
MLP	2.16	4.71	31.40	3.13 (0.74)	31.68(31.63)	33.29 (8.75)
SPDNet	0.20	1.08	0.73	0.43 (0.18)	0.68 (0.27)	1.09 (0.25)
CMNN	0.30	0.68	0.71	0.47 (0.12)	1.22 (0.92)	1.16 (0.26)

Table 3: Normalised and per-sample norms of the neural networks with the scaling uncertainty dataset.

Model	L1 (Sam-ple)	L2 (Sam-ple)	L ∞ (Sam-ple)	L1 (Mean)	L2 (Mean)	L ∞ (Mean)	L1 (Std)	L2 (Std)	L ∞ (Std)
MLP	$1.52e^{-4}$	$6.33e^{-6}$	$8.49e^{-4}$	$1.87e^{-4}$	$7.17e^{-6}$	$7.20e^{-4}$	$4.42e^{-4}$	$1.64e^{-5}$	$3.69e^{-3}$
SPDNet	$1.64e^{-4}$	$6.55e^{-6}$	$7.75e^{-4}$	$0.38e^{-4}$	$1.51e^{-6}$	$5.37e^{-4}$	$1.92e^{-4}$	$0.74e^{-5}$	$0.80e^{-3}$
CMNN	$0.78e^{-4}$	$3.33e^{-6}$	$6.69e^{-4}$	$0.44e^{-4}$	$1.94e^{-6}$	$2.60e^{-4}$	$3.58e^{-4}$	$1.323e^{-5}$	$2.03e^{-3}$

to a lesser extent, SPDNet (Fig.(4b)) exhibit larger fluctuations compared to CMNN (Fig.(4c)). This behaviour suggests a tendency for the MLP and, to some extent, SPDNet to over-fit the training set rather than learn the input-output relationship effectively.

Fig.(5-6) shows the errors of the MLP, SPDNet, and CMNN architectures in approximating the temperature field under scaling uncertainty. The first row, Fig.(5a-5c), displays the relative error in a random sample, highlights significant errors, particularly in regions with steep temperature gradients along the diagonal, where variability is highest. SPDNet demonstrates a smoother and more uniform error distribution, though localised areas of elevated errors remain. CMNN shows the lowest relative errors, with minimal and uniformly distributed relative errors across the domain. The second and third rows, Fig.(5d-5i), show the absolute and relative errors in the mean, following a similar trend. Errors are highest for the MLP, concentrated near the patch at $(-0.025, 0)$. CMNN shows lower errors, mainly across the diagonal, while SPDNet achieves the smallest overall errors. The fourth and fifth rows, Fig.(5j-6a), illustrate absolute and relative errors in the standard deviation. Here, SPDNet is generally more accurate. The final row examines the KL divergence, comparing the predicted and reference temperature field distributions. The MLP exhibits scattered and high divergences, while SPDNet and CMNN show significantly lower errors, particularly in high-variance regions.

Overall, SPDNet and to a slightly lesser extent the CMNN outperform the standard MLP when working with scaling uncertainty.

4.1.2. Surrogate model for orientation uncertainty

To investigate neural network performance under orientation uncertainty, we model the eigenvectors as uncertain using Eq.(2.14). The von Mises-Fisher distribution obtained from Eq.(2.15), is shown in Fig.(7), illustrating the directional concentration of samples around the reference vector. In this visualization, the reference vector $\boldsymbol{\mu}$ is defined as the first column of the eigenvector matrix specified in Eq.(4.1). A concentration parameter of $\eta = 200$ characterises the spread of the distribution

Fig.(8) illustrates the reference solution under orientation uncertainty, as randomisation of principal directions leads to localised changes in heat flow alignment. The mean temperature field, depicted in

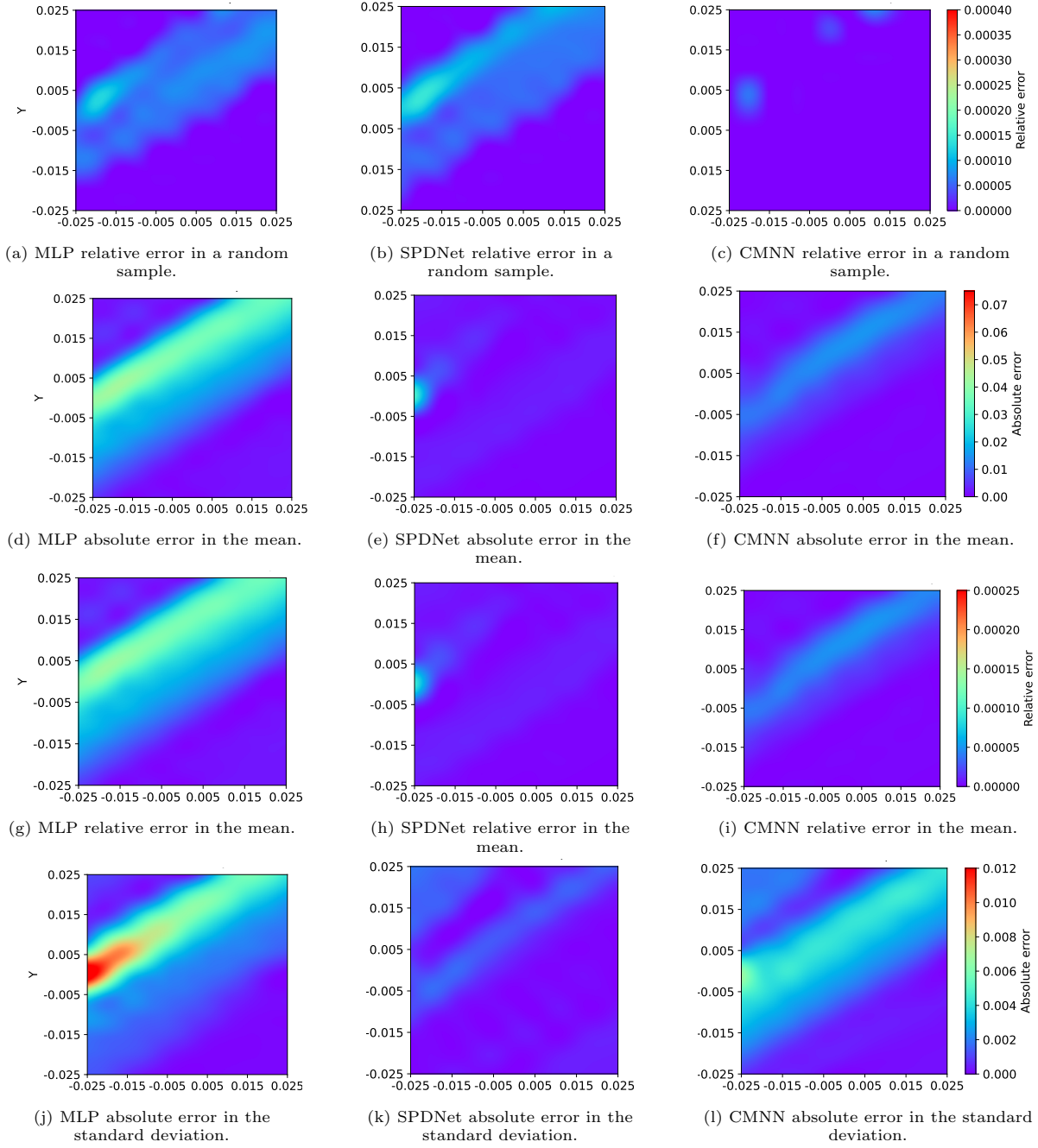


Figure 5: Errors in approximation of the temperature field by the neural networks with the scaling uncertainty dataset.

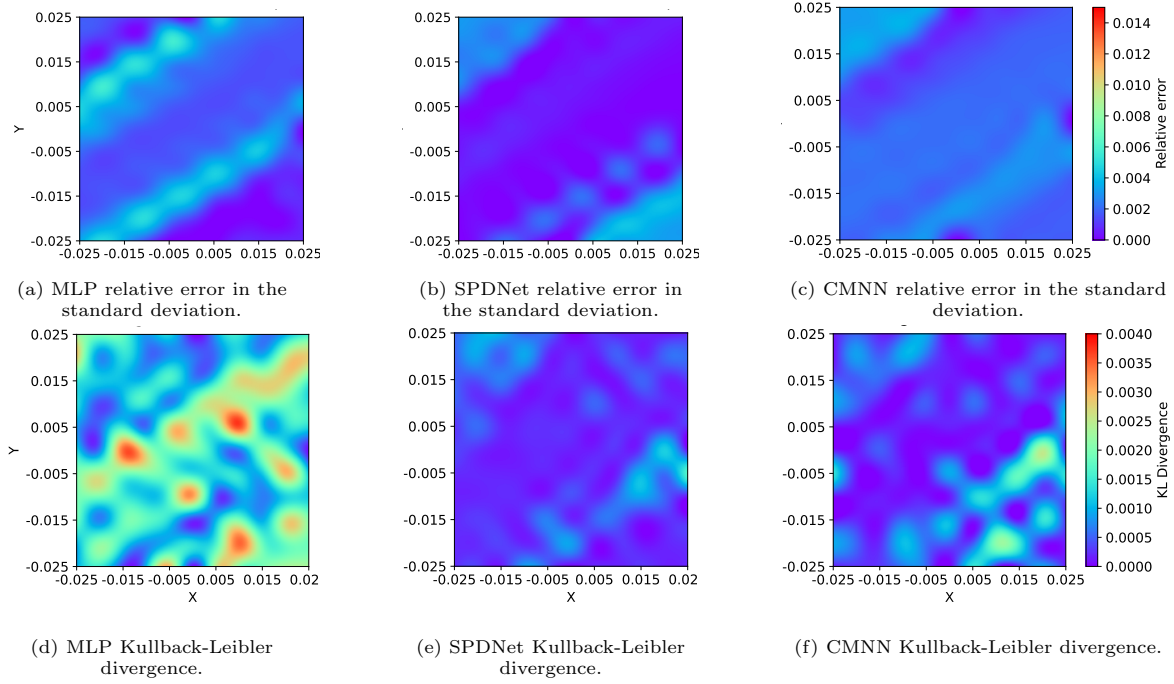


Figure 6: Errors in approximation of the temperature field by the neural networks with the scaling uncertainty dataset.

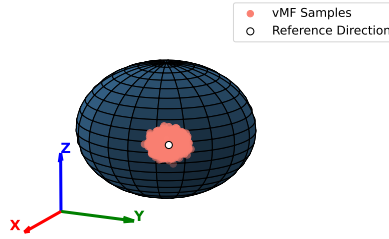


Figure 7: Von mises fisher distribution with $\eta = 200$.

Fig.(8a), aligns closely with the deterministic solution. The standard deviation, shown in Fig.(8b), reveals lower uncertainty near the entry patch at $(-0.025, 0)$, where the gradient direction is largely preserved. However, further from the entry point, uncertainty increases as heat flows toward the patches at $(0, 0.025)$ and $(0.025, 0)$, reflecting the effects of orientation variability.

The influence of orientation is even more pronounced in Fig.(8e) and Fig.(8f), which depict the lower (5%) and upper (95%) angle percentile temperature fields, respectively. The lower-angle field shows clear deviations from the mean, with noticeable shifts in heat distribution. The upper-angle field exhibits even greater changes, emphasizing the sensitivity of the temperature field to orientation variations. This behaviour is further reflected in the probability distributions presented in Fig.(8c), where orientation uncertainty leads to significant variations in the statistical characteristics of the temperature

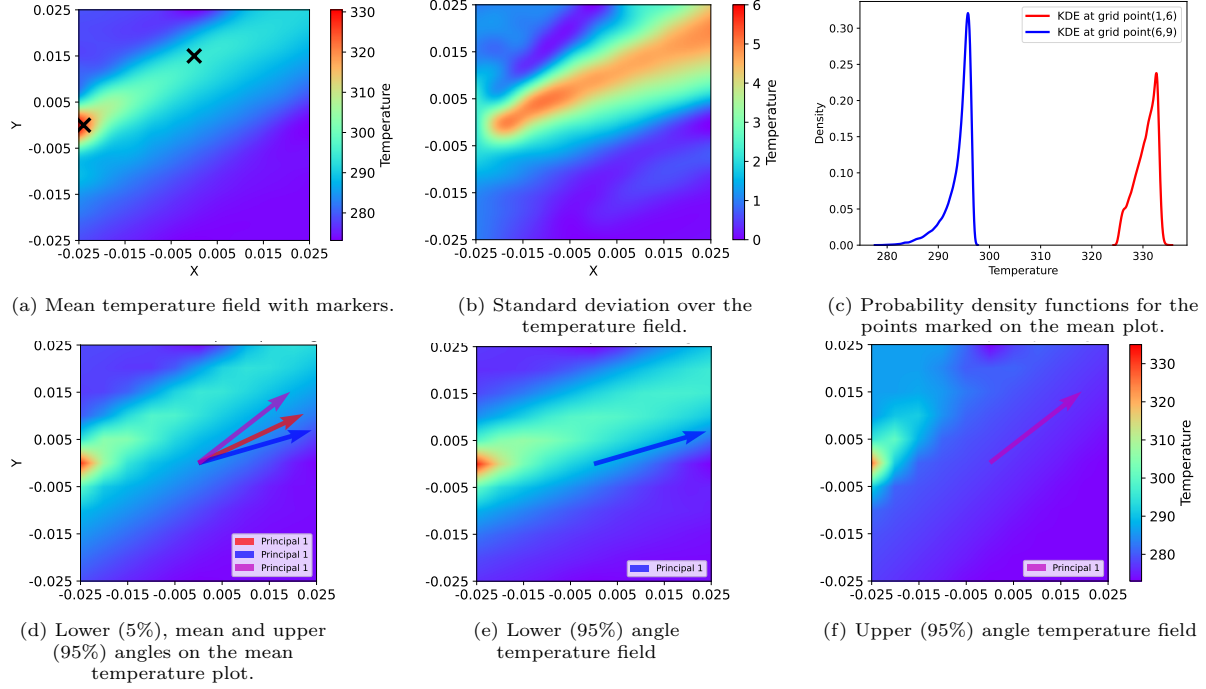


Figure 8: Temperature field statistics in the XY plane with the orientation uncertainty dataset.

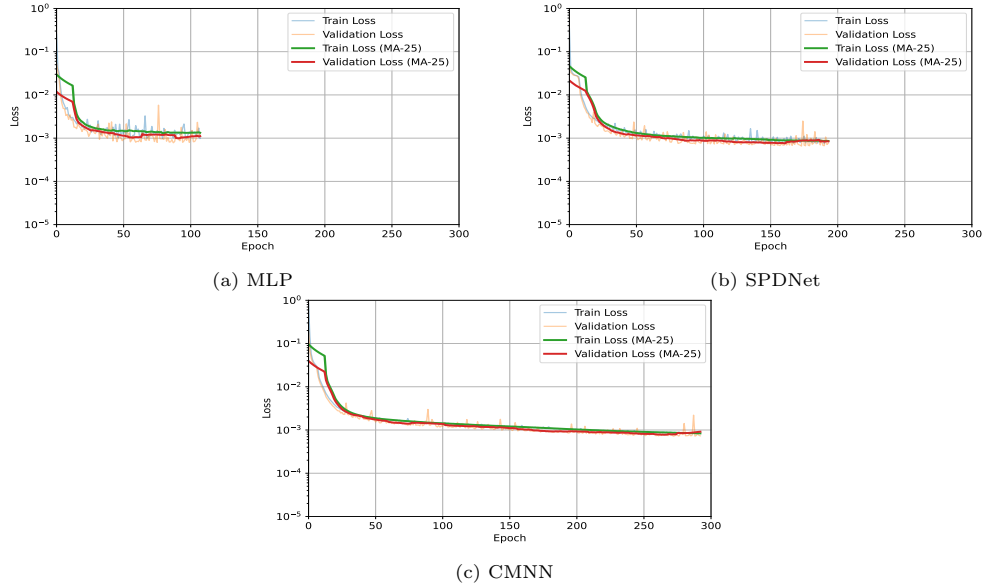


Figure 9: Training history of the neural networks with the orientation uncertainty dataset.

field. Compared to scaling uncertainty, orientation-driven variability causes more spatially distributed heat transport.

To train the networks, the optimised hyper-parameters were 500 epochs, a batch size of 32, hidden layers of sizes 32 and 8, a sigmoid activation function, and a learning rate of $7.5 \times e^{-3}$. Table 4 summarises the training performance of the MLP, SPDNet and CMNN architectures on the random-orientation data set. Although the performance gaps are smaller than in the scaling-uncertainty case, the MLP again shows slightly lower consistency and accuracy. SPDNet exhibits the smallest variation, particularly in the validation loss, whereas CMNN attains the lowest test and training losses. All three models perform consistently across the ten repeated experiments. The normalised per-sample norms in Table 5 show that CMNN consistently outperforms SPDNet and, in particular, the MLP. In Fig.(9), a similar phenomenon to that seen in the scaling-uncertainty training histories appears: the MLP displays the most erratic behaviour, SPDNet is smoother, and CMNN remains the most stable, although it requires more epochs to converge.

Fig.(10-11) illustrates the errors in approximating the temperature field under orientation uncertainty for the MLP, SPDNet and CMNN architectures. The relative errors in Fig.(10a) remain generally low for all three models, with only minor local variations. The absolute and relative errors in the mean temperature field—shown in Fig.(10d–10i)—and in the standard deviation—depicted in Fig.(10j–11c)—reveal that the MLP produces the largest errors along the high-temperature diagonal, while SPDNet exhibits noticeable mean and standard-deviation errors in the upper-right corner. The final row, focusing on the Kullback–Leibler divergence in Fig.(11d–11f), shows elevated values for all models in regions where the probability-density functions have high kurtosis, as seen in Fig.(8f).

Overall, CMNN displays the most stable and consistent training behaviour under orientation uncertainty, followed by SPDNet and, lastly, the MLP.

Table 4: Training metrics of the neural networks with the orientation uncertainty dataset. Data in magnitude order of e^{-4} .

Layer	Best Loss	Val. Loss	Test Loss	Train Loss	Mean Loss (Std.)	Val. Loss (Std.)	Mean Loss (Std.)	Test Loss (Std.)	Mean Loss (Std.)	Train Loss (Std.)
MLP	7.79		10.16	13.12	8.6 (0.8)		14.1 (5.8)		12.2 (1.7)	
SPDnet	6.54		8.79	8.23	7.1 (0.4)		9.5 (1.7)		9.1 (1.5)	
CMNN	7.18		8.37	7.75	8.0 (0.8)		9.3 (2.0)		9.5 (1.3)	

Table 5: Normalised and per-sample norms of the neural networks with the orientation uncertainty dataset.

Model	L1 (Sam- ple)	L2 (Sam- ple)	L ∞ (Sam- ple)	L1 (Mean)	L2 (Mean)	L ∞ (Mean)	L1 (Std)	L2 (Std)	L ∞ (Std)
MLP	$5.02e^{-4}$	$2.22e^{-5}$	$6.78e^{-3}$	$3.54e^{-4}$	$1.44e^{-5}$	$1.71e^{-3}$	$1.84e^{-3}$	$7.03e^{-5}$	$1.15e^{-2}$
SPDNet	$2.34e^{-4}$	$1.03e^{-5}$	$2.97e^{-3}$	$1.32e^{-4}$	$0.63e^{-5}$	$1.85e^{-3}$	$1.08e^{-3}$	$4.67e^{-5}$	$1.24e^{-2}$
CMNN	$1.76e^{-4}$	$0.85e^{-5}$	$2.69e^{-3}$	$1.12e^{-4}$	$0.54e^{-5}$	$1.13e^{-3}$	$0.63e^{-3}$	$2.90e^{-5}$	$0.67e^{-2}$

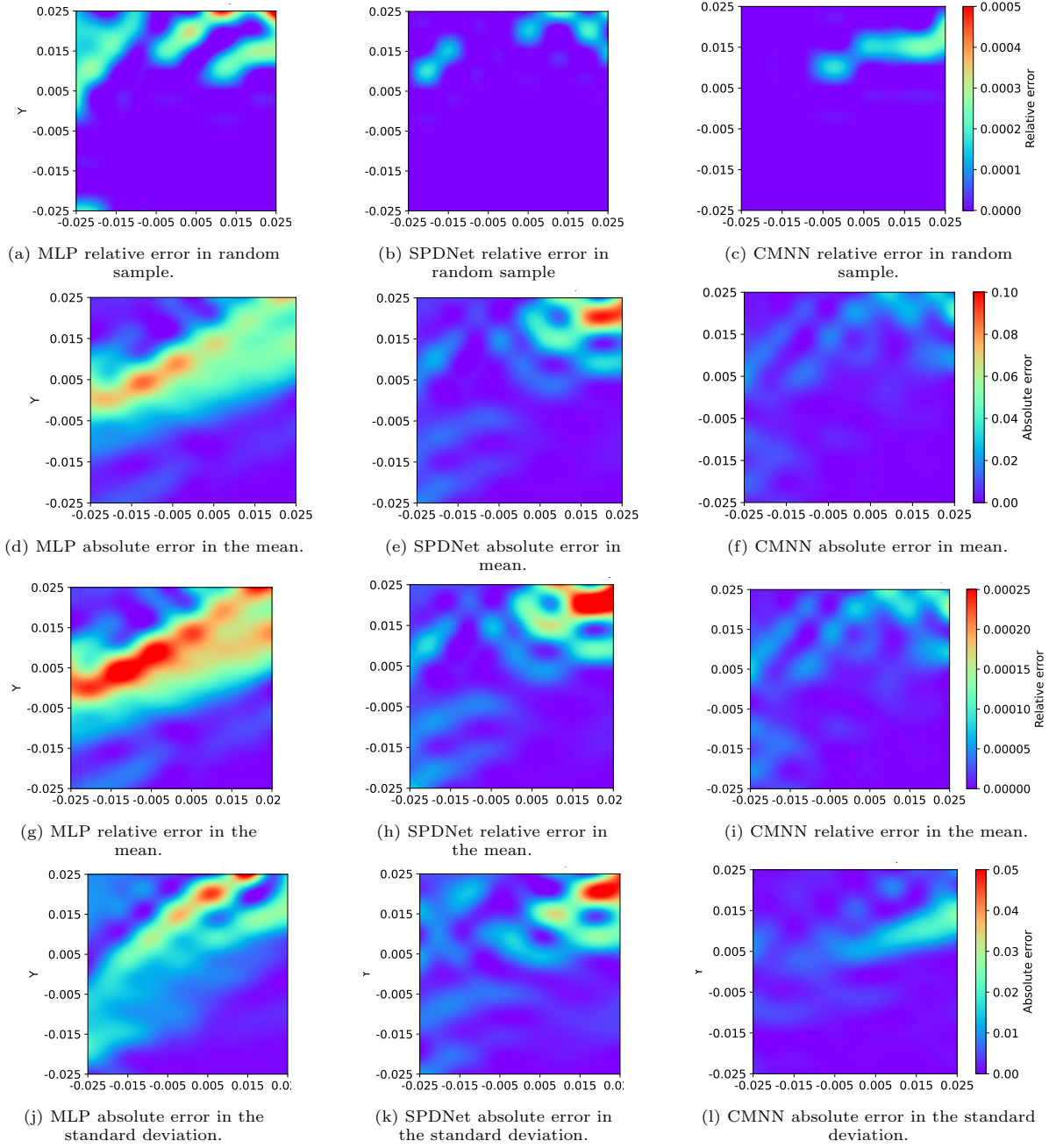


Figure 10: Errors in approximation of the temperature field by the neural networks with the orientation uncertainty dataset.

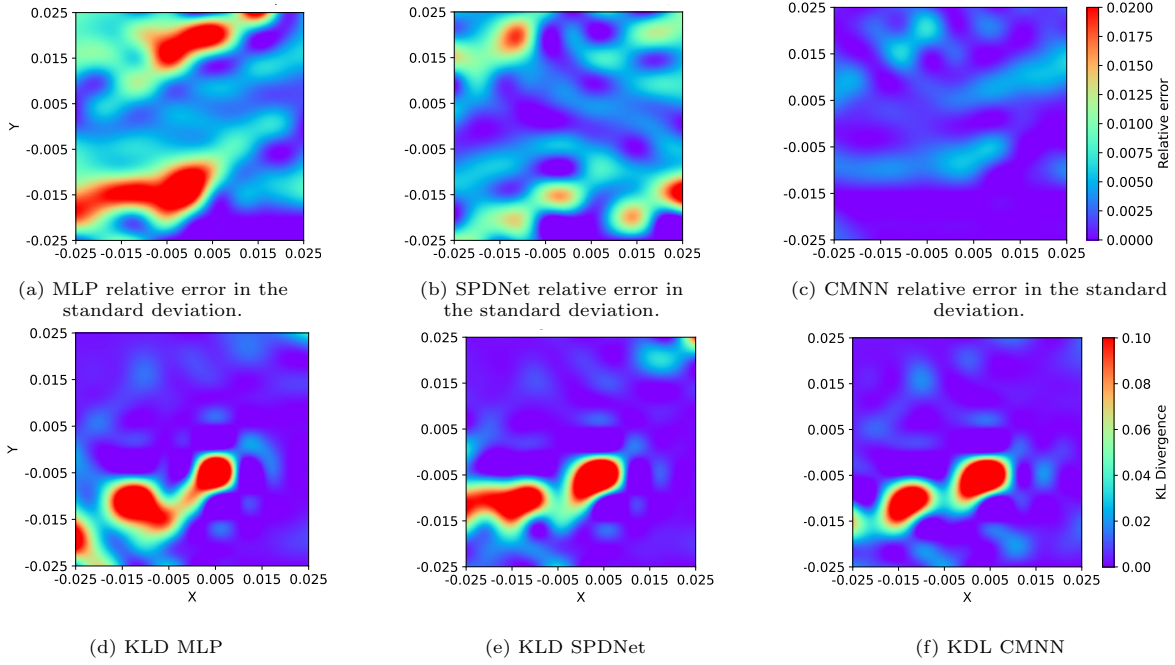


Figure 11: Errors in approximation of the temperature field by the neural networks with the orientation uncertainty dataset.

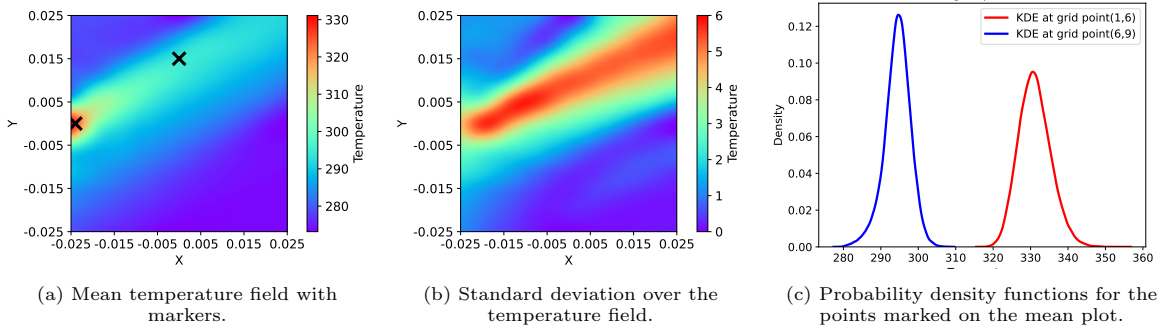


Figure 12: Temperature field statistics in the XY plane with the combined scaling-orientation uncertainty dataset.

4.1.3. Surrogate model for the combined scaling-orientation uncertainty

To test the neural networks under combined scaling and orientation uncertainty, we combine the random-scaling and random-orientation parameters from Eq.(2.11). These six random variables are detailed in Table 1 and visualised in Fig.(7). The reference results appear in Fig.(12). The mean temperature field in Fig.(12a) closely matches the deterministic solution. The standard deviation in Fig.(12b) reflects the combined effects of scaling and orientation. Its pattern resembles the sum of the standard deviations from the pure-orientation case (Fig.(8b)) and the pure-scaling case (Fig.(3b)). Finally, Fig.(12c) shows the probability-density functions at two marked points; these distributions have greater spread and are

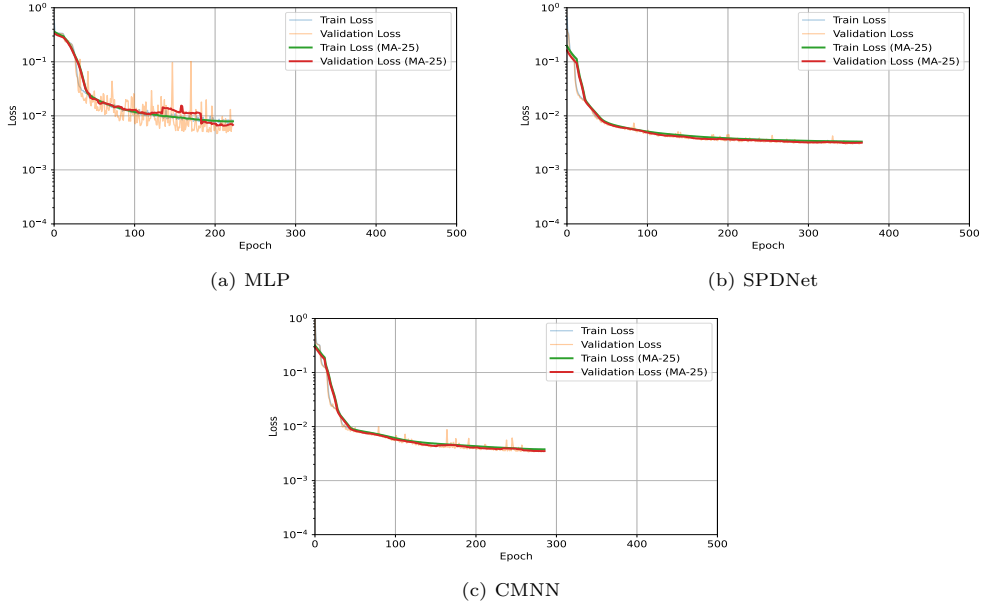


Figure 13: Training history of the neural networks with the combined scaling-orientation uncertainty dataset.

nearer to a normal shape, since the combined uncertainty reduces the influence of any single source and mitigates skewness.

For the MLP, SPDNet and CMNN architectures the optimised hyper-parameters are 300 epochs, a batch size of 16, three hidden layers of sizes 48, 16 and 8, a sigmoid activation function, a learning rate

Table 6: Training metrics of the neural networks with the combined scaling-orientation uncertainty dataset. Data in magnitude order of e^{-3} .

Layer	Best Loss	Val. Test Loss	Train Loss	Mean Val. Loss (Std.)	Mean Test Loss (Std.)	Mean Train Loss (Std.)
MLP	4.68	7.02	8.17	6.46 (1.15)	8.69 (2.27)	9.35 (1.16)
SPDnet	2.98	3.42	3.34	3.43 (0.21)	3.45 (0.27)	3.47 (0.23)
CMNN	3.38	3.77	3.89	3.74 (0.33)	3.77 (0.25)	3.83 (0.21)

Table 7: Normalised and per-sample norms of the neural networks with the combined scaling-orientation uncertainty dataset.

Model	L1 (Sample)	L2 (Sample)	L ∞ (Sample)	L1 (Mean)	L2 (Mean)	L ∞ (Mean)	L1 (Std)	L2 (Std)	L ∞ (Std)
MLP	$2.42e^{-3}$	$9.3e^{-5}$	$19.1e^{-3}$	$11.5e^{-4}$	$4.5e^{-5}$	$7.1e^{-3}$	$6.57e^{-3}$	$23.7e^{-5}$	$25.9e^{-3}$
SPDNet	$1.83e^{-3}$	$7.5e^{-5}$	$15.7e^{-3}$	$2.94e^{-4}$	$1.1e^{-5}$	$1.86e^{-3}$	$0.94e^{-3}$	$3.5e^{-5}$	$7.36e^{-3}$
CMNN	$2.54e^{-3}$	$10.2e^{-5}$	$18.7e^{-3}$	$2.85e^{-4}$	$1.1e^{-5}$	$1.42e^{-3}$	$1.29e^{-3}$	$5.7e^{-5}$	$14.2e^{-3}$

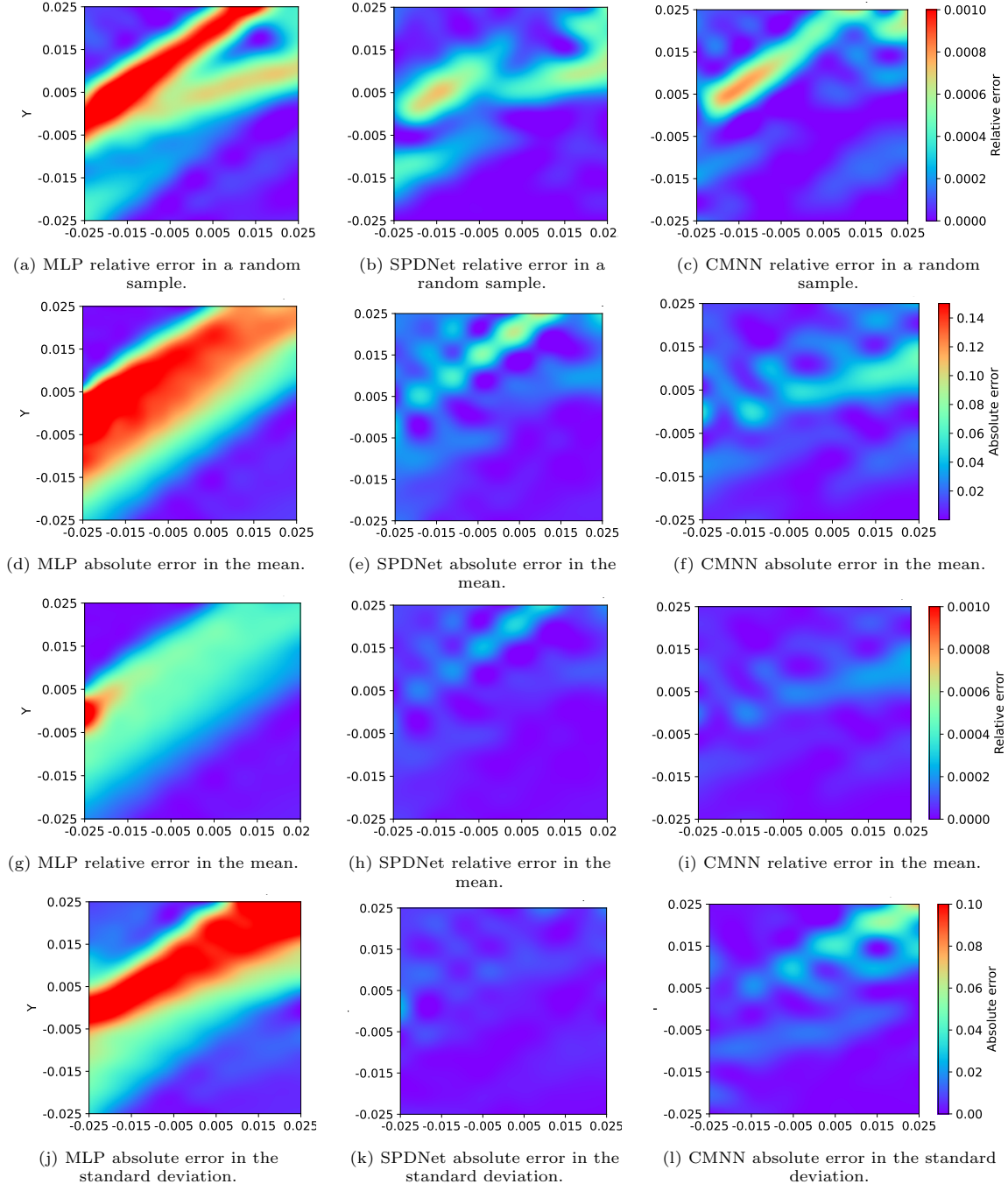


Figure 14: Errors in approximation of the temperature field by the neural networks with the combined scaling-orientation uncertainty dataset.

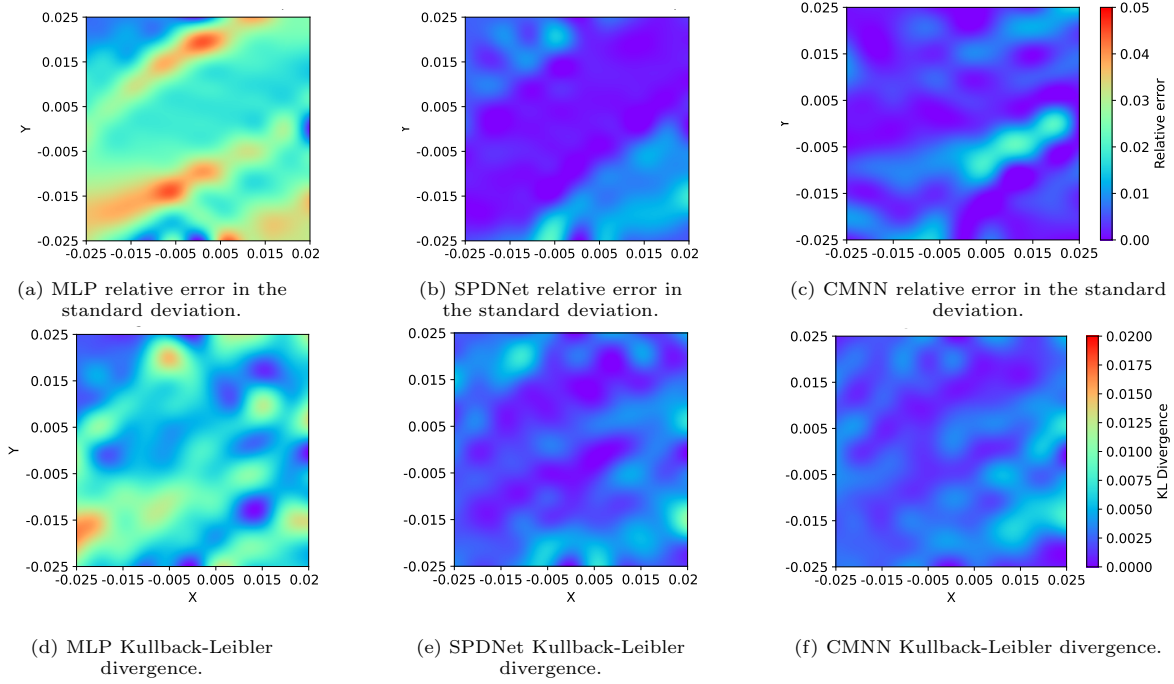


Figure 15: Errors in approximation of the temperature field by the neural networks with the combined scaling-orientation uncertainty dataset.

of $2.5 \times e^{-3}$ and the Adam optimiser. Table 6 shows their training, validation and test losses on the combined scaling-and-orientation data set. Note that these losses lie in the order of e^{-3} rather than e^{-4} .

The MLP exhibits the highest variability and poorest performance, with a best validation loss of $4.68 \times e^{-3}$, a test loss of $7.02 \times e^{-3}$ and a training loss of $8.17 \times e^{-3}$. Its mean validation and test losses, $6.46 \times e^{-3}$ and $8.69 \times e^{-3}$ respectively, and their standard deviations underscore its inconsistency. Between CMNN and SPDNet the differences are smaller, with SPDNet slightly outperforming CMNN across all metrics. As in the scaling-uncertainty case (Table 3), SPDNet edges out in estimating the standard deviation.

The training history for the neural networks under combined scaling and orientation uncertainty is shown in Fig.(13). The MLP, Fig.(13a), exhibits noticeable instability during training, with significant fluctuations in both training and validation losses. In contrast, SPDNet shown in Fig.(13b) and CMNN shown in Fig.(13c) display considerably more stable convergence, with smoother loss curves throughout training.

Fig.(14–15) presents the errors in approximating the temperature field under combined scaling and orientation uncertainty for the MLP, SPDNet, and CMNN architectures. In a random sample, the relative errors shown in Fig.(14a - 14c) for the MLP are noticeably higher compared to SPDNet and CMNN, particularly in regions with high temperature gradients. This trend persists in both the absolute and relative errors of the mean seen in Fig.(14d–14i) and the absolute and relative errors of the standard deviation in Fig.(14j–15c), where the MLP exhibits greater inaccuracies. The Kullback–Leibler (KL) divergence shown in Fig.(15d - 15f) further highlights these discrepancies, with SPDNet showing localised areas of higher divergence, likely due to inaccuracies in approximating the mean in those regions.

In contrast, CMNN and MLP exhibit slightly higher divergence in specific regions; however, CMNN maintains better overall consistency compared to both the MLP and SPDNet.

In summary, both geometry-aware models surpass the standard MLP on the combined-uncertainty dataset. SPDNet achieves the lowest validation errors, and CMNN matches it closely on the test set while retaining smooth training behaviour.

4.1.4. Case study discussion

Across the three case studies, one recurring issue is the reliability of the validation loss as an indicator of generalisation performance. When the validation set happens to align closely with patterns the network has learned, the loss can be over-optimistic and lower than the true error on the full data set. Selecting the model with the smallest validation loss therefore amounts to cherry-picking. Part of the mismatch also stems from using the mean-squared-error loss, which does not always capture meaningful differences for outputs that reside in stochastic spaces. For comparing predicted distributions, divergence measures such as the Kullback–Leibler divergence or the Wasserstein distance better reflect discrepancies in statistical structure.

Using one set of shared hyper-parameters for all architectures may have limited individual performance. The Bayesian optimisation was run with equal weighting across the MLP, SPDNet and CMNN, and it tended to favour the weakest model rather than unlocking the full potential of each. Separate hyper-parameter searches would probably improve results for individual networks. Additional techniques such as drop-out or batch normalisation could further stabilise training, but they were excluded here to keep the comparison focused on the three input maps: flattening for the MLP, LogEig for SPDNet and StrAng for CMNN.

The training curves in Fig.(4), Fig.(9) and Fig.(13) where a good indicator of generalisation performance. CMNN and SPDNet show smooth, stable convergence under every uncertainty type, whereas the MLP fluctuates markedly. Together with the norm tables and field-wise error plots, these histories provide a clear picture of global and local behaviour. From these sources it can be concluded that CMNN performed best with orientation uncertainty and SPDNet performed best with scaling uncertainty, both clearly benefitting from manifold-aware preprocessing. The standard MLP lagged behind, especially in approximating probability distributions.

5. Conclusion

This work investigates three neural network architectures for physics-based problems involving uncertain symmetric positive-definite tensors. The proposed methods differ in how they preserve the relationship between samples in the input space while mapping from the tensor manifold to the Euclidean space in which neural networks operate. These architectures are employed to approximate the function defined in Eq.(2.5), where the stochastic tensor model is specified by Eq.(2.11). In the case study, MLP, SPDNet, and CMNN are evaluated for their ability to approximate this function under scaling, orientation, and combined uncertainties. Both the newly formulated CMNN and the SPDNet, which is introduced here in the context of physics-based problems, outperform the MLP in terms of training stability and accuracy, as demonstrated in the previous section. These results highlight the potential of CMNN and SPDNet in effectively handling SPD material properties for function approximation tasks, making them promising candidates for uncertainty-aware machine learning in physics-based applications.

The case study focuses on a relatively simple physical problem with predominantly linear behaviour. In more complex scenarios involving nonlinear physics, such as multi-physics interactions or heterogeneous materials, the advantages of architectures like SPDNet and CMNN could become even more

pronounced. These methods may offer greater robustness in capturing intricate dependencies that standard MLPs struggle to describe effectively. Additionally, the observed differences between SPDNet and CMNN are relatively minor in this study, with the CMNN edging out on in uncertainty propagations performance for orientation uncertainty, possibly due to the matrix logarithm used for the eigenvectors.

While neural networks offer scalability and efficiency, they also face inherent challenges such as limited interpretability, sensitivity to hyperparameter choices, and occasional instability, as seen for the MLP network. These limitations highlight the continued importance of numerical solvers for solving physics-based problems, as the approximation of the function can only be as good as the underlying data from which it originates.

This work demonstrates that embedding geometric representations of SPD tensors into neural networks leads to more accurate and robust uncertainty quantification. By extending beyond traditional Euclidean mappings, this framework contributes to more robust surrogate modelling of stochastic materials and offers new opportunities for computational material science.

References

- [1] D. L. Corwin and E. Scudiero, “Field-scale apparent soil electrical conductivity,” *Soil Science Society of America Journal*, vol. 84, no. 5, pp. 1405–1441, 2020. [_eprint: https://onlinelibrary.wiley.com/doi/pdf/10.1002/saj2.20153](https://onlinelibrary.wiley.com/doi/pdf/10.1002/saj2.20153).
- [2] H. Ahmadi Moghaddam and P. Mertiny, “Stochastic Finite Element Analysis Framework for Modelling Mechanical Properties of Particulate Modified Polymer Composites,” *Materials*, vol. 12, p. 2777, Jan. 2019. Number: 17 Publisher: Multidisciplinary Digital Publishing Institute.
- [3] G. B. Saturnino, A. Thielscher, K. H. Madsen, T. R. Knösche, and K. Weise, “A principled approach to conductivity uncertainty analysis in electric field calculations,” *NeuroImage*, vol. 188, pp. 821–834, Mar. 2019.
- [4] J. C. Kolecki, “An Introduction to Tensors for Students of Physics and Engineering,” *Glenn Research Center*, 2002.
- [5] S. Siengchin, “A review on lightweight materials for defence applications: Present and future developments,” *Defence Technology*, vol. 24, pp. 1–17, June 2023.
- [6] R. Leijsen, W. Brink, C. van den Berg, A. Webb, and R. Remis, “Electrical Properties Tomography: A Methodological Review,” *Diagnostics*, vol. 11, p. 176, Feb. 2021. Number: 2 Publisher: Multidisciplinary Digital Publishing Institute.
- [7] S. Chen, D. Arrouays, V. Leatitia Mulder, L. Poggio, B. Minasny, P. Roudier, Z. Libohova, P. Lagacherie, Z. Shi, J. Hannam, J. Meersmans, A. C. Richer-de Forges, and C. Walter, “Digital mapping of *GlobalSoilMap* soil properties at a broad scale: A review,” *Geoderma*, vol. 409, p. 115567, Mar. 2022.
- [8] M. Itskov, *Tensor Algebra and Tensor Analysis for Engineers: With Applications to Continuum Mechanics*. Mathematical Engineering, Cham: Springer International Publishing, 2015.
- [9] W. J. Schuttert, M. I. Abdul Rasheed, and B. Rosić, “Modeling variability of the electrical conductivity tensor for the induction welding of composites,” *Proceedings in Applied Mathematics & Mechanics*, 2024. [In press].

- [10] S. K. Shivanand, B. Rosić, and H. G. Matthies, “Stochastic modelling of symmetric positive definite material tensors,” *Journal of Computational Physics*, vol. 505, p. 112883, May 2024.
- [11] J. Zhang, “Modern Monte Carlo methods for efficient uncertainty quantification and propagation: A survey,” *WIREs Computational Statistics*, vol. 13, no. 5, p. e1539, 2021. eprint: <https://onlinelibrary.wiley.com/doi/pdf/10.1002/wics.1539>.
- [12] C. Lataniotis, *Data-driven uncertainty quantification for high-dimensional engineering problems*. phdthesis, ETH Zurich, Nov. 2019.
- [13] R. Schürer, “A comparison between (quasi-)Monte Carlo and cubature rule based methods for solving high-dimensional integration problems,” *Mathematics and Computers in Simulation*, vol. 62, pp. 509–517, Mar. 2003.
- [14] G. Mahdavi and M. A. Hariri-Ardebili, “Kriging, Polynomial Chaos Expansion, and Low-Rank Approximations in Material Science and Big Data Analytics,” *Big Data*, Apr. 2023. Publisher: Mary Ann Liebert, Inc., publishers.
- [15] B. Sudret, S. Marelli, and J. Wiart, “Surrogate models for uncertainty quantification: An overview,” in *2017 11th European Conference on Antennas and Propagation (EUCAP)*, pp. 793–797, Mar. 2017.
- [16] Z. Yin, R. Orozco, M. Louboutin, and F. J. Herrmann, “Solving multiphysics-based inverse problems with learned surrogates and constraints,” *Advanced Modeling and Simulation in Engineering Sciences*, vol. 10, p. 14, Oct. 2023.
- [17] M. Abdar, F. Pourpanah, S. Hussain, D. Rezazadegan, L. Liu, M. Ghavamzadeh, P. Fieguth, X. Cao, A. Khosravi, U. R. Acharya, V. Makarenkov, and S. Nahavandi, “A review of uncertainty quantification in deep learning: Techniques, applications and challenges,” *Information Fusion*, vol. 76, pp. 243–297, Dec. 2021.
- [18] R. K. Tripathy and I. Bilonis, “Deep UQ: Learning deep neural network surrogate models for high dimensional uncertainty quantification,” *Journal of Computational Physics*, vol. 375, pp. 565–588, Dec. 2018.
- [19] M. Lutter, C. Ritter, and J. Peters, “Deep Lagrangian Networks: Using Physics as Model Prior for Deep Learning,” July 2019. arXiv:1907.04490 [cs, eess, stat].
- [20] M. Cranmer, S. Greydanus, S. Hoyer, P. Battaglia, D. Spergel, and S. Ho, “Lagrangian Neural Networks,” July 2020. arXiv:2003.04630.
- [21] M. Raissi, P. Perdikaris, and G. E. Karniadakis, “Physics-informed neural networks: A deep learning framework for solving forward and inverse problems involving nonlinear partial differential equations,” *Journal of Computational Physics*, vol. 378, pp. 686–707, Feb. 2019.
- [22] K. Linka, M. Hillgärtner, K. P. Abdolazizi, R. C. Aydin, M. Itskov, and C. J. Cyron, “Constitutive artificial neural networks: A fast and general approach to predictive data-driven constitutive modeling by deep learning,” *Journal of Computational Physics*, vol. 429, p. 110010, Mar. 2021.
- [23] K. Xu, D. Z. Huang, and E. Darve, “Learning constitutive relations using symmetric positive definite neural networks,” *Journal of Computational Physics*, vol. 428, p. 110072, Mar. 2021.

- [24] K. Linka and E. Kuhl, “A new family of Constitutive Artificial Neural Networks towards automated model discovery,” *Computer Methods in Applied Mechanics and Engineering*, vol. 403, p. 115731, Jan. 2023.
- [25] K. Garanger, J. Kraus, and J. J. Rimoli, “Symmetry-enforcing neural networks with applications to constitutive modeling,” Dec. 2023. arXiv:2312.13511 [cond-mat].
- [26] X. Pennec, P. Fillard, and N. Ayache, *A Riemannian Framework for Tensor Computing*. report, INRIA, 2004. Pages: 34.
- [27] X. Pennec, P. Fillard, and N. Ayache, “A Riemannian Framework for Tensor Computing,” *International Journal of Computer Vision*, vol. 66, pp. 41–66, Jan. 2006.
- [28] P. Buchfink, S. Glas, and B. Haasdonk, “Symplectic Model Reduction of Hamiltonian Systems on Nonlinear Manifolds and Approximation with Weakly Symplectic Autoencoder,” *SIAM journal on scientific computing*, vol. 45, pp. A289–A311, Mar. 2023. Publisher: SIAM.
- [29] Z. Huang and L. Van Gool, “A Riemannian Network for SPD Matrix Learning,” Dec. 2016. arXiv:1608.04233 [cs].
- [30] D. Brooks, O. Schwander, F. Barbaresco, J.-Y. Schneider, and M. Cord, “Riemannian batch normalization for SPD neural networks,” Sept. 2019. arXiv:1909.02414 [cs, stat].
- [31] I. Katsman, E. M. Chen, S. Holalkere, A. Asch, A. Lou, S.-N. Lim, and C. De Sa, “Riemannian Residual Neural Networks,” Oct. 2023. arXiv:2310.10013 [cs, stat].
- [32] R. Chakraborty, M. Banerjee, and B. C. Vemuri, “A CNN for homogeneous Riemannian manifolds with applications to Neuroimaging,” Aug. 2018. arXiv:1805.05487 [cs].
- [33] W. Schuttert, M. I. A. Rasheed, and B. Rosic, “Anisotropy respecting constitutive neural networks,” 9th European Congress on Computational Methods in Applied Sciences and Engineering, ECCOMAS 2024, Oct. 2024.
- [34] L. Onsager, “Reciprocal Relations in Irreversible Processes. I.,” *Physical Review*, vol. 37, pp. 405–426, Feb. 1931. Publisher: American Physical Society.
- [35] J. M. Lee, “Smooth Manifolds,” in *Introduction to Smooth Manifolds* (J. M. Lee, ed.), pp. 1–29, New York, NY: Springer, 2003.
- [36] J. Gallier and J. Quaintance, *Differential Geometry and Lie Groups: A Computational Perspective*, vol. 12 of *Geometry and Computing*. Cham: Springer International Publishing, 2020.
- [37] A. Feragen and A. Fuster, “Geometries and Interpolations for Symmetric Positive Definite Matrices,” in *Modeling, Analysis, and Visualization of Anisotropy* (T. Schultz, E. Özarslan, and I. Hotz, eds.), (Cham), pp. 85–113, Springer International Publishing, 2017.
- [38] K. V. Mardia and P. E. Jupp, *Directional Statistics*. Chichester: John Wiley & Sons, Ltd, 2000.
- [39] C. E. Shannon, “A mathematical theory of communication,” *The Bell System Technical Journal*, vol. 27, pp. 379–423, July 1948. Conference Name: The Bell System Technical Journal.

- [40] E. T. Jaynes, “Information Theory and Statistical Mechanics,” *Physical Review*, vol. 106, pp. 620–630, May 1957. Publisher: American Physical Society.
- [41] V. Arsigny, P. Fillard, X. Pennec, and N. Ayache, “Geometric Means in a Novel Vector Space Structure on Symmetric Positive-Definite Matrices,” *SIAM Journal on Matrix Analysis and Applications*, vol. 29, pp. 328–347, Jan. 2007.
- [42] M. Harandi, M. Salzmann, and R. Hartley, “Dimensionality Reduction on SPD Manifolds: The Emergence of Geometry-Aware Methods,” May 2016. arXiv:1605.06182 [cs].
- [43] Y. Ollivier, “Riemannian metrics for neural networks I: feedforward networks,” Feb. 2015. arXiv:1303.0818 [cs, math].
- [44] A. Schwartzman, *Random ellipsoids and false discovery rates: statistics for diffusion tensor imaging data*. PhD thesis, Stanford University, Jan. 2006.
- [45] A. Schwartzman, “Lognormal Distributions and Geometric Averages of Symmetric Positive Definite Matrices,” *International Statistical Review*, vol. 84, no. 3, pp. 456–486, 2016. eprint: <https://onlinelibrary.wiley.com/doi/pdf/10.1111/insr.12113>.
- [46] P. Gouin O’Shaughnessey, M. Dubé, and I. Fernandez Villegas, “Modeling and experimental investigation of induction welding of thermoplastic composites and comparison with other welding processes,” *Journal of Composite Materials*, vol. 50, pp. 2895–2910, Sept. 2016.
- [47] *COMSOL Multiphysics® v. 6.2*.
- [48] T. Akiba, S. Sano, T. Yanase, T. Ohta, and M. Koyama, “Optuna: A Next-generation Hyperparameter Optimization Framework,” July 2019. arXiv:1907.10902 [cs].
- [49] Y. Buser, G. Bieleman, W. Grouve, S. Wijskamp, and R. Akkerman, “Characterisation of Orthotropic Electrical Conductivity of Unidirectional C/PAEK Thermoplastic Composites,” in *Proceedings of the 20th European Conference on Composite Materials - Composites Meet Sustainability*, pp. 83–91, Ecole Polytechnique Fédérale de Lausanne, 2022.
- [50] W. J. B. Grouve, F. Sacchetti, E. J. Vrugink, and R. Akkerman, “Simulating the induction heating of cross-ply C/PEKK laminates – sensitivity and effect of material variability,” *Advanced Composite Materials*, vol. 30, pp. 409–430, Sept. 2021. Publisher: Taylor & Francis eprint: <https://doi.org/10.1080/09243046.2020.1783078>.